Ion irradiation induced crystalline disorder accelerates interfacial phonon conversion and reduces thermal boundary resistance

Thomas W. Pfeifer[1,*] Henry Aller,[2,†] Eric R. Hoglund[3] Ethan A. Scott[1,4] John A. Tomko[1] Habib Ahmad[5,6] Alan Doolittle,[5,‡] Ashutosh Giri,[7,§] Khalid Hattar[4,8,‖] Alan J. H. McGaughey[2,¶] and Patrick E. Hopkins[1,3,9,#]

[1]*Department of Mechanical and Aerospace Engineering, University of Virginia, Charlottesville, Virginia 22904, USA*
[2]*Department of Mechanical Engineering, Carnegie Mellon University, Pittsburgh, Pennsylvania 15213, USA*
[3]*Department of Materials Science and Engineering, University of Virginia, Charlottesville, Virginia 22904, USA*
[4]*Sandia National Laboratories, Albuquerque, New Mexico 87185, USA*
[5]*School of Electrical and Computer Engineering, Georgia Institute of Technology, Atlanta, Georgia 30332, USA*
[6]*Center for Advanced Electronics & Photovoltaic Engineering, IIUI Islamabad*
[7]*Department of Mechanical, Industrial and Systems Engineering, University of Rhode Island, Kingston, Rhode Island 02881, USA*
[8]*Department of Nuclear Engineering, University of Tennessee, Knoxville, Tennessee 37996, USA*
[9]*Department of Physics, University of Virginia, Charlottesville, Virginia 22904, USA*

(Received 4 April 2023; revised 15 December 2023; accepted 7 March 2024; published 11 April 2024)

Traditional understanding of the thermal boundary resistance (TBR) across solid-solid interfaces posits that the vibrational densities of states overlap between materials dictates interfacial energy transport, with phonon scattering occurring at the interface. Using atomistic simulations, we show a mechanism for control of TBR; point defects near an interface can lead to both short- and midrange disorder, accelerating the conversion of vibrational energy between bulk and interfacial modes, ultimately reducing the TBR. We experimentally demonstrate this reduction through ion irradiation of gallium nitride and subsequently measuring the TBR across Al/GaN interfaces.

DOI: 10.1103/PhysRevB.109.165421

I. INTRODUCTION

The phonon thermal boundary resistance (TBR) across solid-solid interfaces is traditionally considered to depend on the vibrational mismatch of the materials comprising the interface [1–3]. Whether scattering occurs across the interface (diffuse mismatch model) [1] or whether vibrational waves are merely transmitted or reflected (acoustic mismatch model) [4,5], historical theories posit that the difference in populated vibrational density of states (vDOS) is directly correlated to the interfacial resistance. This theory has not always held up in experiments or simulations, however.

For the most part, atomic manipulation of the interfacial structure has resulted in increases in TBR, as demonstrated both computationally [6–8] and experimentally [1,9–13]. However, several works have offered computationally guided predictions into how to reduce TBR with interfacial structure and defects based on the premise of overlapping vDOS. For example, the addition of either discrete or intermixed layers between materials can offer an intermediate vDOS, serving as a bridge and assisting the conversion of heat between the vibrational modes on either side [10,14–16]. Other research has shown that interfacial roughening can achieve similar results via the same mechanism. Roughening produces a mixed-composition region enhancing this phonon bridging effect, and can additionally yield a greater surface area between materials [17,18]. Another theory points to vibrational scattering as the mechanism by which heat is converted between two vibrational populations [19,20], meaning variations in TBR can be explained by calculating the correlations between vibrational modes [21], and TBR can be reduced by enhancing the scattering across the interface [22,23].

Irradiation specifically has also been shown to reduce experimentally measured TBR via these aforementioned computationally guided mechanisms. Gorham *et al.* [24] pointed to the bridging effect as leading to a reduction in TBR across aluminum/native oxide/silicon boundaries following proton irradiation. Similarly, Giri *et al.* [25] exposed superlattices to a N_2 plasma during growth and identified the nitrogen defect-specific vibrational modes as contributing to a decrease in the net thermal resistivity. Finally, discrepancies between theoretical predictions and experiment have occasionally been explained via the cleaning procedures used, as the bonding between layers has been shown to be critical in determining TBR [2]. Follow-up studies on atomically smooth and ultraclean interfaces have resolved some of these discrepancies [20,26].

More recently, numerous authors have developed models wherein the vibrational scattering within the materials adjacent to the interface is considered to affect TBR [21,27–35]. Just as differing bulk vibrational populations result in

*twp4fg@virginia.edu
†Current address: Department of Mechanical Engineering, University of Maryland, College Park, Maryland 20742, USA.
‡alan.doolittle@ece.gatech.edu
§ashgiri@uri.edu
‖khattar@utk.edu
¶mcgaughey@cmu.edu
#peh4v@virginia.edu

a thermal resistance across the interface, differing bulk and interfacial populations will result in additional resistances associated with the decay or thermalization of modes. Duda *et al.* [27] found better agreement in temperature trends between analytical models and molecular dynamics (MD) simulations by incorporating scattering within the material on either side of the interface rather than at the infinitesimally thin interfacial plane only. Wu and Luo [28] found that by increasing the anharmonic terms of their MD potential, even far from the interface, they could reduce TBR. They suggested that this was due to increased energy exchange between modes. Le *et al.* [31] modified the interatomic potential, and suggested that anharmonic processes far from the interface could dominate heat flow. Shi *et al.* [30] modeled heat flow between graphene and carbon nanotubes, identifying the need to decompose the total junction resistance into interfacial components and a boundary region where additional scattering occurs. Murakami *et al.* [29] also noted the influence of inelastic vibrational scattering within a finite-thickness interfacial layer. Next, Gordiz and Henry [21] noted the presence of long-range effects in nonequilibrium MD (NEMD) simulations, suggesting transport effects beyond the interface may play a role in TBR. Finally, Lee and Luo [32] simulated the effects of isotopes, finding that isotope scattering, even at distances away from the interface, could theoretically be used to reduce TBR.

Beyond MD, Boltzmann transport equations or the simplified McKelvey-Shockley flux methods have also been used. For example, Maassen *et al.* [33] explored diffusive and ballistic transport near a Si-Ge interface, showing inelastic bulk scattering occurs near an interface where phonons are out of equilibrium. Green's function models have also been used, such as in the works of Guo *et al.* [34], showing that anharmonicity within a volumetric interfacial region plays a critical role in interfacial thermal transport. Hopkins *et al.* [35] developed a quasiharmonic analytical model for TBR, including volumetric expansion effects, showing that anharmonicity in the materials adjacent to the interface can drive decreases in TBR through changes in the crystal volume.

To our knowledge, no experimental works have demonstrated TBR reductions due to scattering within the material adjacent to the interface. While few prior works have demonstrated that interfacial defects can reduce TBR, pinpointing the role of defects near the interface on the reduction in TBR is still left to computation. For example, the native oxide layer seen by Gorham *et al.* [24] prevents their data from being used to help validate the more recent computational works on the anharmonic and defect proximity effects on TBR. Similarly, the study on amorphous multilayers by Giri *et al.* [25] may not directly translate to predictions from MD simulations at individual crystalline interfaces.

In this paper, we present an experimental study of the TBR across Al/ion-bombarded gallium nitride (GaN) interfaces. GaN is bombarded with varying doses of C^+, N^+, and Ga^{3+} ions, targeting a maximum near-interface defect density of 2%. We show a reduction in the measured Al/GaN TBR. To explain this reduction, we perform MD simulations on a simplified toy system. We use void and interstitial defect pairs in a toy silicon/heavy silicon system to model the defects formed by ion implantation and quantify the resulting crystalline disorder with Procrustes shape analysis [36]. Our results show an increased level of scattering within the defected material due to an increase in short- and midrange crystalline disorder. This assists in the thermalization between interfacial and bulk vibrational modes, resulting in decreases in TBR. This is in contrast to conventional formalisms, where scattering at the interface is said to dominate thermal transport.

II. EXPERIMENTS AND EXPERIMENTAL RESULTS

A. Sample preparation and data analysis

We grow GaN films via metal organic chemical vapor deposition, which we then bombard with varying doses of carbon, gallium, and nitrogen ions (see Table I in the Supplemental Material [37]). An aluminum transducer is then deposited on each sample, and we use time-domain thermoreflectance (TDTR) [38] to measure the TBR across the aluminum/ion-bombarded GaN film interface. In a TDTR measurement, a pulsed laser is used to heat the sample (pump) and subsequently measure the pump-induced temperature rise (probe). The time delay between the arrival of the pump and probe pulses is varied to allow reconstruction of a thermal decay curve, and the data set is fitted to an analytical thermal model. This model consists of a solution to the heat equation in cylindrical coordinates, for an arbitrary layered structure, solved in the frequency domain [38,39] for periodic surface heating and a semi-infinite medium (where the sample geometry is substantially larger than the heated volume), and a fourier series used to analyze in the time domain [38,40]. The layered structure assumed in our model is based on the sample stack, consisting of the aluminum transducer, irradiated GaN, AlN/sapphire substrate (details on properties are listed in Table S2).

We choose ion energies such that the ion stopping ranges (predicted via Stopping and Ranges of Ions in Matter (SRIM) [41] software) exceed the TDTR measurement depth, and we choose doses targeting a ∼2% near-surface defect concentration for our highest-dose samples. A schematic of the irradiated sample and deposited aluminum layer is shown in Fig. 1. Two samples sets were prepared using separate surface cleaning procedures [alcohol cleaning and a more thorough ultrahigh vacuum (UHV) procedure] and growth conditions for the aluminum [e-beam evaporation, and molecular beam epitaxy (MBE)]. Additional details on GaN growth, prediction of ion and defect distributions, surface cleaning procedures, and aluminum growth, can be found in the Supplemental Material [37].

To ensure the measured TBR trend is not an artifact of changes in thermal conductivity (κ), both parameters are fitted with the thermal model [38], and we use contour analysis to calculate uncertainty. This involves comparing the analytical model's decay curve against the data for a range of κ and TBR values. All combinations of κ and TBR which yield satisfactory fits are accepted, and this forms the bounds for the fitted values. We also fit each data set using the ratio of the locked-in in-phase and out-of-phase signal (as is typical for TDTR) and magnitude signal simultaneously. This allows overlapping of contours for a given data set, reducing the uncertainty associated with the measurement [25,42–45]. An

TABLE I. We present the thermal boundary resistance values and vDOS overlap for various monolayers for NEMD simulations without defects and simulations in which defects were added to the heavy silicon or silicon regions. A direct comparison between values for each simulation is presented in the fith and sixth rows.

	TBR	Area overlap: (%)		
Simulation	(m^2 K GW^{-1})	±8 ML	±2 ML	±1 ML
Baseline[A]	16.2	42.8	48.2	57.3
Defects in heavy Si[B]	7.3	45.7	49.5	58.2
Defects in Si[C]	5.7	43.4	50.2	57.5
B–A	−8.9	2.9	1.3	0.9
C–B	−1.6	−2.3	0.7	−0.7

example fit and contour uncertainty is shown in Figs. 2(a) and 2(b).

B. Experimental results

Experimental results are shown in Fig. 3(a) for both sample sets, and a trend in nominally fitted TBR values is observed for both. For the samples subjected to alcohol cleaning and e-beam aluminum, we found TBR values in the range of 9 − 13 m^2 K GW^{-1}, whereas the more thorough UHV-cleaned and MBE-grown aluminum samples yielded lower TBR values by roughly a factor of 4. Once rigorous uncertainty was considered, only the trend in the latter sample set was maintained. Total uncertainty is calculated from geometric mean of the contour uncertainty and the standard deviation between multiple measurements.

Surface roughness and interfacial mixing have both been shown to lead to a decrease in TBR in certain situations [8,12,14,17,24,46–49], so, to check for these effects, we perform scanning transmission electron microscopy (STEM).

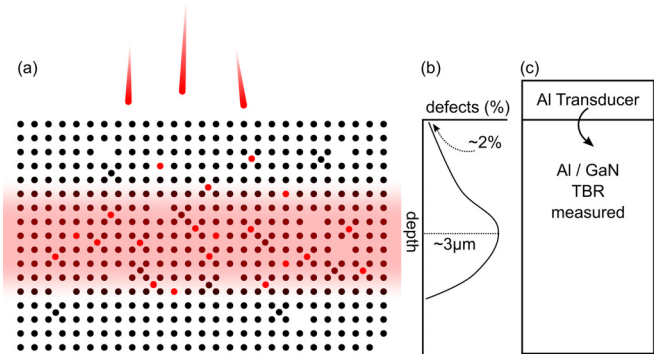

FIG. 1. (a) Illustration of irradiation and resulting point defects (voids, interstitials, substitutional, etc.). (b) A qualitative distribution of irradiation-induced defects is shown; ions induce damage near the surface and come to a stop deeper within the sample. In our experiments, GaN is irradiated with varying doses of C^+, N^+, Ga^{3+} ions (see Supplemental Material [37]. We chose the maximum irradiation dose for each ion so as to target a predicted (via SRIM [41]) near-surface damage level of 2%, and we chose the irradiation energy to ensure the ion stopping depth exceeded 3 μm. This reduces assumptions required in our TDTR analysis. (c) An aluminum transducer is then deposited on the sample, and the TBR across the Al/GaN interface is measured.

High angle annular dark field (HAADF) images were taken at 200 kV on C^+ irradiated samples from the UHV-cleaned and MBE aluminum set [Figs. 3(b) and 3(c)]. We find a ∼2 nm interlayer between the aluminum/GaN, which is present across all samples on which STEM was performed. Note that this interlayer is neglected for the thermal analysis (no additional layer is modeled), as TDTR is unable to differentiate the resistances of extremely thin layers from TBRs (detailed discussion available in the Supplemental Material [37]). We also find no discernible differences in surface roughness or crystallinity despite measuring different TBRs. Similarly, the influence of the GaN heat capacity must be evaluated to ensure any potential radiation effects on heat capacity are not responsible for our measured trend in TBR. After perturbing the GaN heat capacity by 10% and refitting the data, only negligible changes in TBR are found. This is best understood through an inspection of the sensitivity plots [39] [Figs. 2(c) and 2(d)], where the sensitivity to heat capacity is identical or nearly identical to the sensitivity to thermal conductivity. This implies that any error in the heat capacity (due to irradiation) would affect the fitted value for thermal conductivity rather than TBR. Seeking an explanation for the surprising decrease in TBR, we next turn to simulations.

III. SIMULATIONS AND COMPUTATIONAL RESULTS

A. Computational setup

We perform nonequilibrium molecular dynamics (NEMD) simulations using LAMMPS (Large-scale Atomic/Molecular Massively Parallel Simulator) [50] on a Stillinger-Weber (SW) silicon (28.0855 g/mol)/heavy silicon (72.64 g/mol) system. We introduce interstitial and void pairs (Frenkel defects) by pseudorandomly selecting and displacing atoms, since we expect crystalline disorder to be the primary near-interface effect of irradiation [51–54]. As we are more interested in the qualitative effects defects have on TBR and the vibrational properties in and around the interface rather than material-specific properties, our simplified simulations, choice of computational domain, and use of the SW potential should suffice, while allowing direct comparison to other literature. We also choose Frenkel defects for the sake of simplicity and since domain size limitations within MD complicate the addition of other types of crystalline defects. We

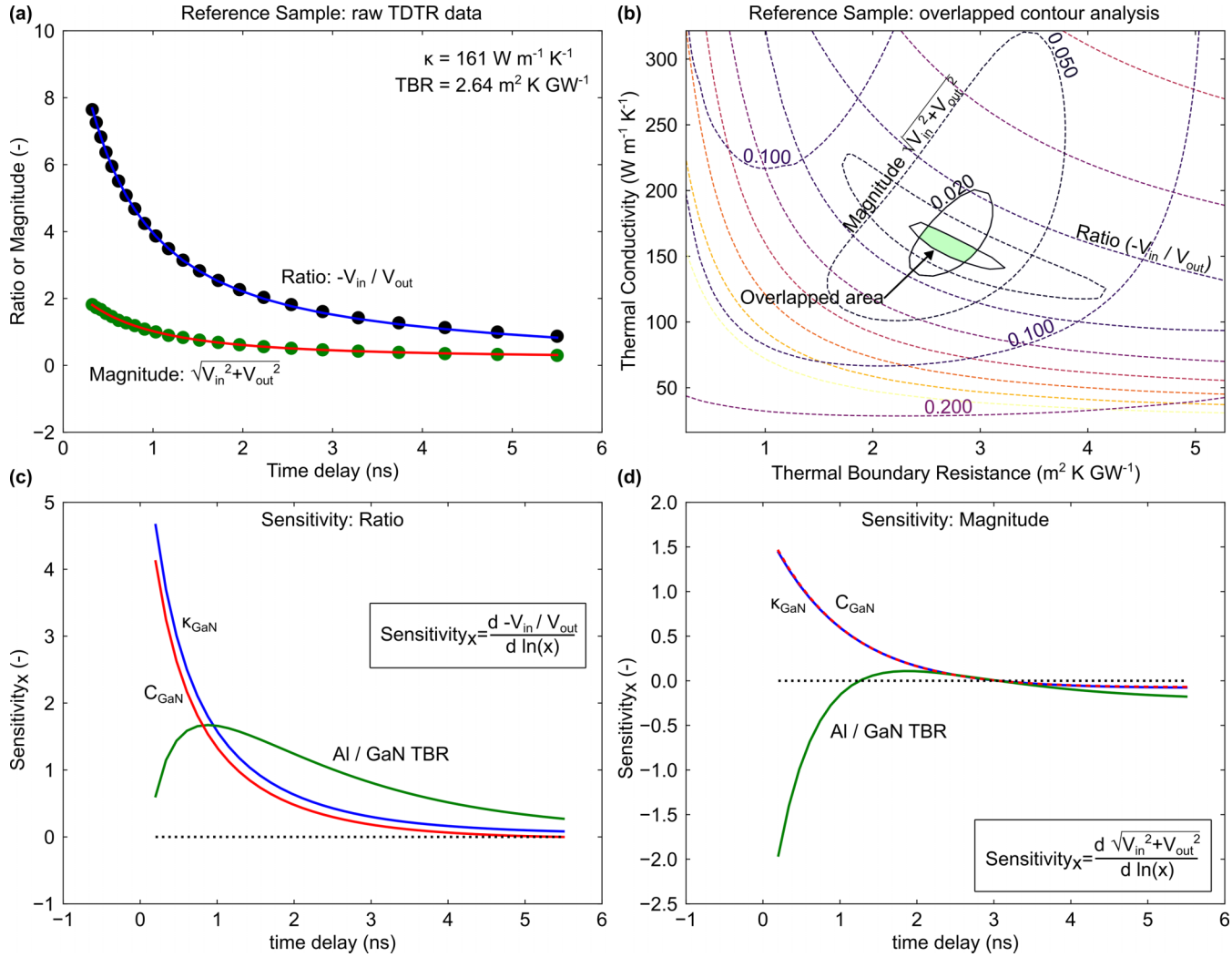

FIG. 2. (a) An example of raw TDTR data is shown, fitting for both the ratio of in-phase (V_{in}) and out-of-phase (V_{out}) data (as is typical) and the signal magnitude. This has the advantage of allowing overlapped contour analysis (b). The quality of fit between data and model is checked across the full parameter space (all combinations of κ and TBR), and contours are drawn to denote a given quality of fit. Only combinations of values which yield satisfactory fits (2% residual) for both ratio and magnitude data are accepted (overlapped region). To ensure radiation effects on heat capacity do not affect our results, we perturb the GaN heat capacity and refit, noting negligible changes in fitted TBR values. This is best understood through sensitivity analysis [39] [(c), (d)], where each parameter is perturbed and the deviation of the model curve is recorded. Heat capacity and thermal conductivity have nearly identical sensitivity, suggesting that an error in heat capacity will affect the fitted thermal conductivity but not the TBR.

chose a concentration of 2% defects to match the predictions for the maximum near-interface defect density from SRIM.

We ran three sets of simulations: a baseline case where no defects were added and simulations in which we added Frenkel defects to the silicon or heavy silicon sides. Defects are added by randomly selecting a set number of atoms in each monolayer (ensuring a uniform defect density through the length of the simulation) and displacing them 2.5 unit cells (minimizing recombination effects). During the initialization, we also perform a psuedoannealing step, wherein we initialize to 1.5× the desired equilibrium temperature and ramp downward using an NVT ensemble. This ensures any defect evolution or recombination occurs at the beginning of the simulation before averaging begins (prior to extraction of TBR or vDOS). We also note that the use of a three-body potential appears to be critical for the preservation of crystalline defects. While other potentials such as Lennard-Jones are more common or computationally efficient, we found a Lennard-Jones argon/krypton system (face center cubic) would either recrystallize or become amorphous after the structural defects were introduced. Further details on the simulation procedure (including exact simulation parameters) can be found in the Supplemental Material [37].

We use Procrustes shape analysis (PSA) for the quantification of crystalline disorder in a similar manner to Han *et al.* [36]. PSA is traditionally used as a quantitative comparison between arbitrary 3D shapes, and we apply this

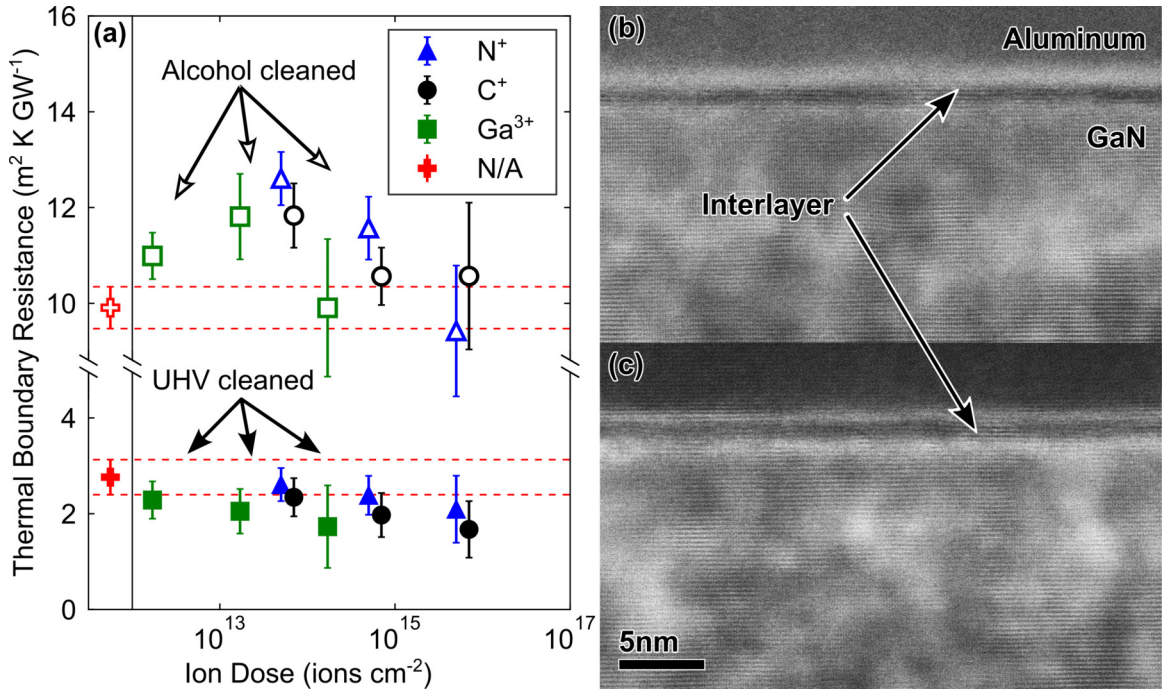

FIG. 3. (a) TBR is measured between an aluminum capping layer and ion-irradiated GaN. Two sample sets are prepared, first using our standard alcohol cleaning and e-beam aluminum deposition procedure (open symbols), and separately using a more rigorous ultrahigh vacuum (UHV) cleaning and MBE deposition process (solid). A trend in nominal TBR values appears for both, with the alcohol-cleaned samples showing TBR values roughly 4× higher. Once rigorous uncertainty is considered, however (calculated via contour analysis and the standard deviation across multiple measurements), the trend is difficult to establish for the alcohol-cleaned samples. By comparison, a trend is clear with the UHV and MBE samples, with a near-universal reduction in TBR following bombardment. STEM images are taken on low- (b) and intermediate- (c) dose C^+ samples within the UHV and MBE sample set, and no significant qualitative differences are seen at the interface to explain the difference in TBR. Both have a ∼2 nm intermediate layer between the Al and GaN.

comparison to the tetrahedrons formed by each atom's four neighboring atoms and lattice sites in the diamond cubic crystal. The comparison is performed by first finding the time-averaged position of each atom, and the four nearest-neighbor atom positions. The Kabsch algorithm is used to calculate the rotation required to align the neighbor atom positions to a regular tetrahedron, and the mean-squared distance of each point to the center is used to calculate scaling. Once alignment of the neighbor positions to the perfect tetrahedral lattice positions is calculated, the Procrustes distance is simply the mean-squared distance between points. This is thus a measurement of the local environment each atom sees and can be used to find atoms of each class (interstitials, neighbors to voids, etc.) in low disorder cases. Similarly, long-range disorder such as the warping of lattice planes can be observed. Additional details on the PSA calculation can be found in the Supplemental Material [37], and further discussion is found below.

B. Simulation results and discussion

In our baseline system with no defects, we found a TBR of 16.2 $m^2\,K\,GW^{-1}$. By adding defects to the silicon or heavy silicon sides, the TBR reduced to 5.7 or 7.3 $m^2\,K\,GW^{-1}$, respectively. A comparison of the vDOS of both regions does not explain the difference in TBR. The bulk vDOS of both silicon and heavy silicon (calculated from the atoms centered between the baths and interface) does not substantially change with the addition of defects, aside from a slight difference in the sharpness of features [Fig. 4(a)]. We also compute the area overlap between both bulk and interfacial vDOS [14,30]. This is related to the harmonic scattering across the interface, meaning an increase in the overlap factor could explain the reduction in TBR (results tabulated in Table I). In some cases (e.g., monolayers half a unit cell from the interface) the vDOS and TBR follow the expected trend to a limited degree (e.g., only a ∼0.9% overlap difference between the baseline and defected heavy silicon cases, despite TBR being less than half). For other cases, however (e.g., bulk vDOS or first monolayers adjacent to the interface, Fig. S6) the expected trend does not hold (higher overlap when defects are added to heavy silicon vs silicon, despite having a higher TBR). Both of these discrepancies suggest that changes in vDOS overlap from the local structure and defects cannot explain the reduction in TBR following irradiation.

We also calculate the spectral heat flux (SHF) between groups of atoms by tracking the velocities of each atom and interatomic forces [22,55–61]. This has been traditionally calculated across interfaces but can also be done for arbitrary

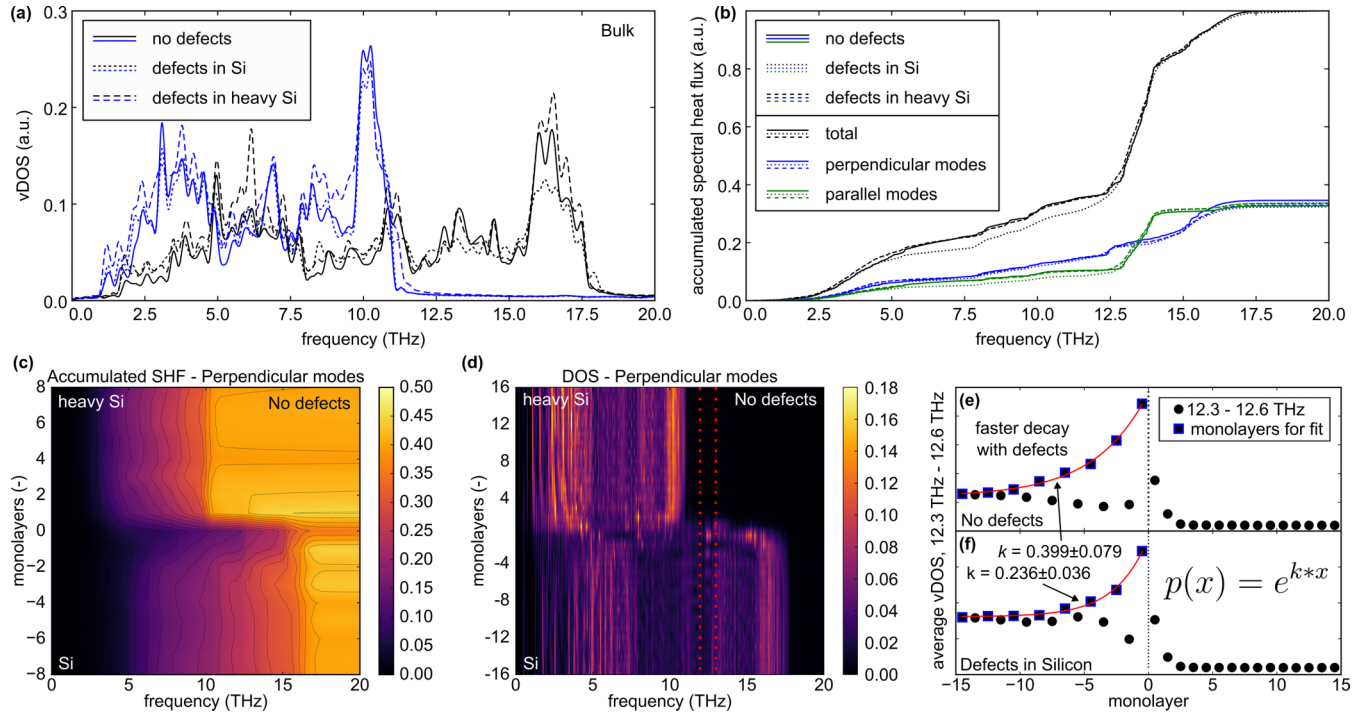

FIG. 4. (a) We calculate the vibrational density of states (vDOS) for the bulk silicon (black) and heavy silicon (blue) sides of our simulation, for the three simulation conditions (undefected: solid; defects in silicon: dotted; and defects in heavy silicon: dashed). We find no clear features to explain the great reduction in TBR. The overlap factor is also calculated (tabulated values available in the Supplemental Material [37]) with no clear trends. (b) We calculate the total accumulated spectral heat flux (SHF) across the interface (black) and shearlike (blue) and transverselike (green) components for all three simulation conditions as well. 12–13 THz vibrations dominate heat flow across the boundary and the contribution of these modes are largely unaffected by the addition of defects. (c) Spatially dependent SHF and (d) spatially dependent vDOS are assembled by simply calculated accumulated SHF [as in (b)] or vDOS [as in (a)] across multiple imaginary planes or for each monolayer within the simulation. A thermalization region is visible where the heat-carrying modes change as the interface is approached. Optical modes affecting every other atomic plane are visible (outlined in red), which we believe result from the interface limiting the vibration of specific atoms. Fitting an exponential to this mode yields a quantifiably different decay rate between the undefected (e) and defected (f) cases.

groups of atoms, e.g., across imaginary planes within the bulk. The SHF across the interface for the undefected case is very similar to that of silicon/germanium, which has been studied before [21,62], where the 12–13 THz interfacial modes dominate heat flow across the interface [Fig. 4(b), presented as an accumulated heat flux as a function of frequency). In the calculation of SHF, the direction of forces and velocities can be used to distinguish between the relative contributions of vibrations parallel to and perpendicular to the interface. Note that we do not call these transverse and longitudinal modes, respectively, as a phonon wave vector is not attainable from these simulations. We note a significant contribution of parallel modes to heat flux across the boundary, and ensure our simulation cross section is sufficiently large so as to not affect these modes. In addition to the 12–13 THz parallel modes, there is also a lesser contribution of perpendicular modes in the 2.5–5, 7–10, and 15–18 THz ranges. Comparing defected and undefected cases, the SHF is similar, with 12–13 THz modes continuing to dominate. All the same modes carry heat in similar proportions as they did in the undefected case, however they are able to carry more vibrational energy across the interface.

Comparing interfacial SHF to vDOS, we note that the 12–13 THz heat-carrying modes do not appear as dominant modes in either bulk vDOS. Similarly, both the 12–13 THz and 15–18 THz frequency ranges are well above the highest vDOS frequencies for the heavy silicon. Instead, high-frequency optical modes of both materials scatter and form these intermediate frequency vibrations ($\sim$16 THz and $\sim$10 THz for silicon and heavy silicon, respectively, forming the 12–13 THz vibrations).

There is also significant overlap of either bulk or interfacial vDOS outside of these 12–13 and 15–18 THz ranges which do not substantially contribute to heat flux (e.g., around $\sim$6 THz). Instead, it is primarily the interfacial modes with significant scattering to other bulk modes which carry the most substantial amounts of heat [21,62]. This is in contrast to the bulk case, where the bulk accumulated SHF and vDOS curves line up (shown in Fig. S7), suggesting that all bulk modes present roughly uniformly carry heat. While not included in the traditional understanding of TBR, we posit the role of the phonon wave vector within each material may be key; phonons may exist in both materials at 6 THz, for example, but may not be momentum-matched across the interface. While

these 6 THz phonons will carry heat within the bulk, scattering would be required to allow these modes to couple and transmit heat across the boundary.

Finally, we investigate the spatial variation of both SHF and vDOS [Figs. 4(c) and 4(d)] by calculating accumulated SHF across many arbitrary slice planes or vDOS for multiple monolayers and presenting as a surface plot. In both SHF and vDOS, some modes are modified as they near the interface. In SHF [Fig. 4(c)], modes between 5–15 THz are lower in magnitude on the silicon side as far as two monolayers from the interface, and the sum of all perpendicular modes is lower across the interface (rightmost intensity). For vDOS [Fig. 4(d)], a direct shifting in frequencies can be observed (e.g., with amplified 15 THz modes appearing adjacent to the interface). This suggests there is a volume where interfacial modes must thermalize into bulk modes. Within this thermalization region, scattering is required to couple the heat-carrying modes between the bulk regions and interface, and the presence of this region is direct evidence that scattering within the medium (not solely across the interface) is occurring. If defects serve to enhance this scattering, better mode conversion would be expected, reducing the overall resistance. Note that additional spatially varying SHF and vDOS images are available in Supplemental Material [37] Figs. S9 and S10.

We suggest that the size of this thermalization region may relate to the scattering rates for the given material. Qualitatively, we can see the SHF transition distance is significantly larger on the silicon side [Fig. 4(c)], in agreement with the notion that scattering times [or phonon mean free paths (MFPs)] should be higher in silicon. This may also explain the greater reduction in TBR when defects are added to silicon vs heavy silicon; if defects enhance the scattering within the material, enhancing the heat flow across the interface and reducing TBR, then this effect is reduced in heavy silicon where scattering rates are already high.

More quantitatively, we also select a narrow band of modes on vDOS and plot the amplitude of the mode as a function of position [Figs. 4(e) and 4(f)]. The modes between 12.3–12.6 THz specifically show an alternating behavior, where every other monolayer experiences this vibration and the amplitude shows a clear decay moving away from the interface. While optical modes would not ordinarily appear nonuniformly within a bulk medium, we suspect this is the product of an interfacial effect (and note that this appeared across a series of simulations, including differing domain sizes and conditions, warranting further study). We fit an exponential function to the alternating monolayers nonetheless, and note a significantly faster decay in the defected simulations (1.7× decay constant between the baseline and defected silicon cases). This comparison of decay rates is possible with other frequency ranges as well, but few are as dramatic as the 12.3–12.6 THz range (which lines up with the dominant heat-carrying modes from SHF as well).

Finally, we also note that parallel SHF modes show a greater contribution to heat flow across the interface vs within the bulk. This suggests that not only do the frequencies of heat-carrying modes change, but so does the direction of vibrational motion.

These observations further support our assertion to reconsider the premise that the overlap of vDOS controls TBR. Instead, scattering within the material adjacent to the interface allows coupling between bulk and interfacial modes, which is a requirement for interfacial heat flow. Stated differently, just as the requirement to convert energy between bulk vDOS populations results in TBR under the traditional explanation, the additional conversion requirement within either medium results in additional thermal resistances if scattering mechanisms are limited.

In their study of amorphous vs crystalline interfaces, Gordiz and Henry [21] also commented on the somewhat counterintuitive relationship between the short MFPs within amorphous materials (leading to low thermal conductivities), and the low TBR across amorphous materials' boundaries. Within the context of mode conversion within the material adjacent to the interface, however, this observation is no longer a surprise; if short MFPs are associated with high scattering rates and better conversion between vibrational modes, short MFPs will result in a lower overall TBR.

Finally, in an effort to understand the nature of the additional scattering as relating to the defects induced, we turn to the Procrustes quantification of disorder [36]. Each atom's four nearest neighbors are found, and the distances of each from their expected lattice sites (forming a tetrahedron) is calculated. This yields a Procrustes distance for each atom [shown in Fig. 5(a)], and specific defect types are visible.

Looking at the distributions of Procrustes distances [Fig. 5(b)], all atoms have a Procrustes distance of less than 3×10^{-5} Å for the undefected case, implying a near-perfect crystalline structure. All atoms are where they should be, the crystal is not strained or deformed, and nonzero Procrustes distances only result from the vibrational motion of the atoms. In the systems with 2% defects, however, Procrustes distances reach as high as 6×10^{-2} Å, with over 50% of atoms (far more than would be accounted for based on the number of added defects) reaching as high as 1.1×10^{-4} Å [Fig. 5(b)]. This implies there is distortion of the lattice, even at a distance from the introduced defects. Furthermore, the angle of rotation or anisotropic scaling parameters used to align each quartet of atoms to a tetrahedral set of lattice sites are also high compared to the undefected case (distribution shown in Fig. S14 in the Supplemental Material [37]). The pristine case sees a maximum rotation angle of 0.2°, while a 0.5° rotation for atoms is common in the defected case (applying to ∼33% of atoms). This suggests there is warpage of atomic planes beyond merely strain (or anisotropic strain for a confined film). Interestingly, similar results are found for varying concentrations of defects [e.g., a simulation with 0.2% defects still yields 26% of atoms with Procrustes distances above the 3×10^{-5} Å undefected maximum or ∼10% of atoms with a >0.5° rotation angle, Fig. 5(b)].

These observations can further explain the experimental results. While localized defects may result from irradiation, additional short- and mid-range crystalline disorder may also be introduced (e.g., the warping of lattice planes around defects). This disorder may not directly affect the vDOS overlap, but it will enhance scattering within the defected medium beyond that caused by the relatively low concentration of defects alone. This result is similar to experimental observations for

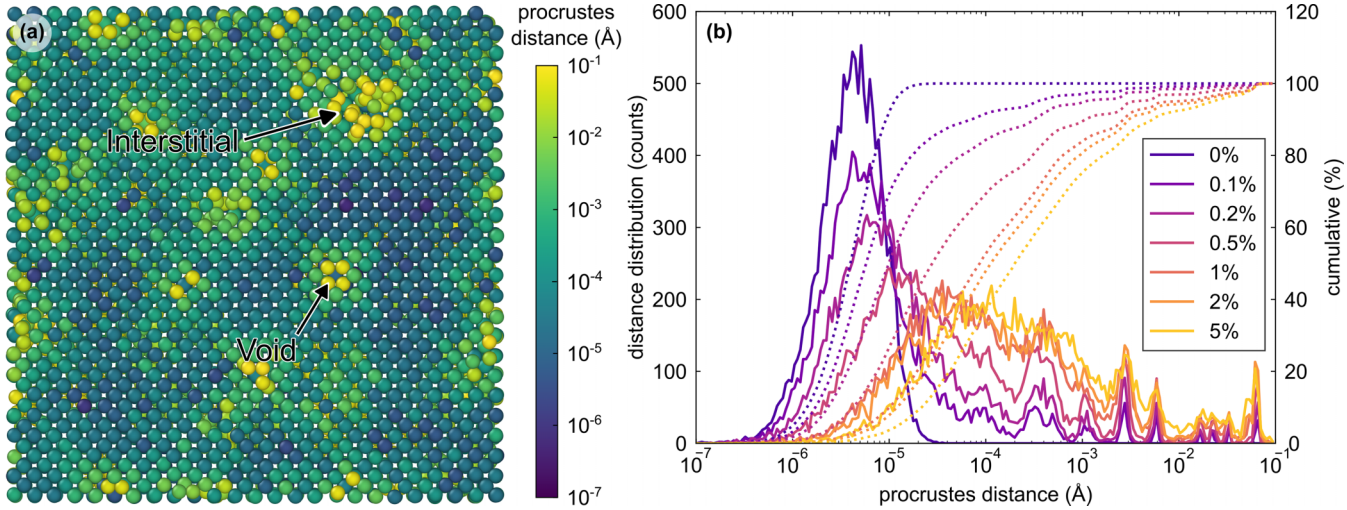

FIG. 5. We compute the Procrustes distances for each atom (used as an indicator of the localized disorder seen by a given atom). (a) A color map of Procrustes distances for a simulation with 2% added defects shows how Procrustes distances are associated with specific defect types. Voids are the most obvious, as an atom is merely missing. The structure associated with interstitials is far less consistent, however, as the relaxation of the system causes multiple atoms to shift out of place. (b) A histogram of Procrustes distances is plotted (solid) for varying defect concentrations. All follow a roughly normal distribution, with peaks appearing which are likely associated with specific defect states. We also present the integration across these distributions (dotted). 50% of atoms in the 2% defects case have Procrustes distances of 1.1×10^{-4} Å or more compared to the undefected case where all atoms are below 3×10^{-5} Å. In other words, a majority of atoms (far more than the nominal density of introduced defects) have a much more distorted local environment. The effects of the (relatively few) defects are not localized to the defects alone, implying the presence of medium- and long-range disorder.

ion irradiated materials [63], where the thermal conductivity is affected by scattering from the localized strain fields associated with defects rather than the defects themselves.

IV. CONCLUSIONS

Additional scattering (both in our experiments and simulations) has been shown to assist in the thermalization of interfacial modes, allowing better energy exchange between populations. This increased energy exchange translates to a reduction in the overall resistance associated with the interface.

This has ramifications on the potential reduction of TBR via the manipulation of crystalline disorder, either via *ex situ* irradiation or in-situ growth (e.g., isotopic disorder). The control of this short- and midrange crystalline disorder provides a mechanism to control mode conversion through the unique vibrational modes that only arise at interfaces. This, coupled with more traditionally employed routes to manipulate TBR based on vDOS overlap or disruption of longer range order (e.g., amorphous layers) could lead to designer interfaces with user-defined phononic TBRs.

ACKNOWLEDGMENTS

We appreciate support from the Office of Naval Research through a MURI program, Grant No. N00014-18-1-2429. We appreciate support from the National Science Foundation, Grant No. 2318576. A.G. acknowledges funding from the Office of Naval Research, Grant No. N00014-21-1-2622. This work was performed, in part, at the Center for Integrated Nanotechnologies, an Office of Science User Facility operated for the U.S. Department of Energy (DOE) Office of Science. Sandia National Laboratories is a multimission laboratory managed and operated by National Technology and Engineering Solutions of Sandia, LLC, a wholly owned subsidiary of Honeywell International, Inc., for the U.S. DOE's National Nuclear Security Administration under Contract No. DE-NA-0003525. The views expressed in the paper do not necessarily represent the views of the U.S. DOE or the United States Government.

[1] E. T. Swartz and R. O. Pohl, Thermal boundary resistance, Rev. Mod. Phys. **61**, 605 (1989).

[2] C. Monachon, L. Weber, and C. Dames, Thermal boundary conductance: A materials science perspective, Annu. Rev. Mater. Res. **46**, 433 (2016).

[3] A. Giri and P. E. Hopkins, A review of experimental and computational advances in thermal boundary conductance and nanoscale thermal transport across solid interfaces, Adv. Funct. Mater. **30**, 1903857 (2020).

[4] I. M. Khalatnikov, Heat exchange between a solid and helium II, J. Exp. Theor. Phys. **22**, 687 (1952).

[5] W. A. Little, The transport of heat between dissimilar solids at low temperatures, Can. J. Phys. **37**, 334 (1959).

[6] W. Ih Choi, K. Kim, and S. Narumanchi, Thermal conductance at atomically clean and disordered silicon/aluminum interfaces: A molecular dynamics simulation study, J. Appl. Phys. **112**, 054305 (2012).

[7] A. Van Roekeghem, B. Vermeersch, J. Carrete, and N. Mingo, Thermal resistance of Ga N/Al N graded interfaces, Phys. Rev. Appl. **11**, 034036 (2019).

[8] J. C. Duda, T. S. English, E. S. Piekos, T. E. Beechem, T. W. Kenny, and P. E. Hopkins, Bidirectionally tuning Kapitza conductance through the inclusion of substitutional impurities, J. Appl. Phys. **112**, 073519 (2012).

[9] T. Beechem and P. E. Hopkins, Predictions of thermal boundary conductance for systems of disordered solids and interfaces, J. Appl. Phys. **106**, 124301 (2009).

[10] J. C. Duda and P. E. Hopkins, Systematically controlling Kapitza conductance via chemical etching, Appl. Phys. Lett. **100**, 111602 (2012).

[11] P. E. Hopkins, L. M. Phinney, J. R. Serrano, and T. E. Beechem, Effects of surface roughness and oxide layer on the thermal boundary conductance at aluminum/silicon interfaces, Phys. Rev. B **82**, 085307 (2010).

[12] P. E. Hopkins, P. M. Norris, R. J. Stevens, T. E. Beechem, and S. Graham, Influence of interfacial mixing on thermal boundary conductance across a chromium/silicon interface, J. Heat Transfer **130**, 062402 (2008).

[13] S. Yang, H. Song, Y. Peng, L. Zhao, Y. Tong, F. Kang, M. Xu, B. Sun, and X. Wang, Reduced thermal boundary conductance in GaN-based electronic devices introduced by metal bonding layer, Nano Res. **14**, 3616 (2021).

[14] T. S. English, J. C. Duda, J. L. Smoyer, D. A. Jordan, P. M. Norris, and L. V. Zhigilei, Enhancing and tuning phonon transport at vibrationally mismatched solid-solid interfaces, Phys. Rev. B **85**, 035438 (2012).

[15] Z. Liang and H. L. Tsai, Effect of thin film confined between two dissimilar solids on interfacial thermal resistance, J. Phys.: Condens. Matter **23**, 495303 (2011).

[16] A. Giri, R. Cheaito, J. T. Gaskins, T. Mimura, H. J. Brown-Shaklee, D. L. Medlin, J. F. Ihlefeld, and P. E. Hopkins, Thickness-independent vibrational thermal conductance across confined solid-solution thin films, ACS Appl. Mater. Interfaces **13**, 12541 (2021).

[17] X. W. Zhou, R. E. Jones, C. J. Kimmer, J. C. Duda, and P. E. Hopkins, Relationship of thermal boundary conductance to structure from an analytical model plus molecular dynamics simulations, Phys. Rev. B **87**, 094303 (2013).

[18] Z. Liang, K. Sasikumar, and P. Keblinski, Thermal transport across a substrate-thin-film interface: Effects of film thickness and surface roughness, Phys. Rev. Lett. **113**, 065901 (2014).

[19] P. E. Hopkins, J. C. Duda, and P. M. Norris, Anharmonic phonon interactions at interfaces and contributions to thermal boundary conductance, J. Heat Transfer **133**, 062401 (2011).

[20] Z. Cheng, Y. R. Koh, H. Ahmad, R. Hu, J. Shi, M. E. Liao, Y. Wang, T. Bai, R. Li, E. Lee, E. A. Clinton, C. M. Matthews, Z. Engel, L. Yates, T. Luo, M. S. Goorsky, W. A. Doolittle, Z. Tian, P. E. Hopkins, and S. Graham, Thermal conductance across harmonic-matched epitaxial Al-sapphire heterointerfaces, Commun. Phys. **3**, 115 (2020).

[21] K. Gordiz and A. Henry, Phonon transport at interfaces between different phases of silicon and germanium, J. Appl. Phys. **121**, 025102 (2017).

[22] K. Sääskilahti, J. Oksanen, J. Tulkki, and S. Volz, Role of anharmonic phonon scattering in the spectrally decomposed thermal conductance at planar interfaces, Phys. Rev. B **90**, 134312 (2014).

[23] Z. Lu, A. M. Chaka, and P. V. Sushko, Thermal conductance enhanced via inelastic phonon transport by atomic vacancies at Cu/Si interfaces, Phys. Rev. B **102**, 075449 (2020).

[24] C. S. Gorham, K. Hattar, R. Cheaito, J. C. Duda, J. T. Gaskins, T. E. Beechem, J. F. Ihlefeld, L. B. Biedermann, E. S. Piekos, D. L. Medlin, and P. E. Hopkins, Ion irradiation of the native oxide/silicon surface increases the thermal boundary conductance across aluminum/silicon interfaces, Phys. Rev. B **90**, 024301 (2014).

[25] A. Giri, S. W. King, W. A. Lanford, A. B. Mei, D. Merrill, L. Li, R. Oviedo, J. Richards, D. H. Olson, J. L. Braun, J. T. Gaskins, F. Deangelis, A. Henry, and P. E. Hopkins, Interfacial defect vibrations enhance thermal transport in amorphous multilayers with ultrahigh thermal boundary conductance, Adv. Mater. **30**, 1804097 (2018).

[26] Y. R. Koh, J. Shi, B. Wang, R. Hu, H. Ahmad, S. Kerdsongpanya, E. Milosevic, W. A. Doolittle, D. Gall, Z. Tian, S.l Graham, and P. E. Hopkins, Thermal boundary conductance across epitaxial metal/sapphire interfaces, Phys. Rev. B **102**, 205304 (2020).

[27] J. C. Duda, P. M. Norris, and P. E. Hopkins, On the linear temperature dependence of phonon thermal boundary conductance in the classical limit, J. Heat Transfer **133**, 074501 (2011).

[28] X. Wu and T. Luo, The importance of anharmonicity in thermal transport across solid-solid interfaces, J. Appl. Phys. **115**, 014901 (2014).

[29] T. Murakami, T. Hori, T. Shiga, and J. Shiomi, Probing and tuning inelastic phonon conductance across finite-thickness interface, Appl. Phys. Express **7**, 121801 (2014).

[30] J. Shi, Y. Dong, T. Fisher, and X. Ruan, Thermal transport across carbon nanotube-graphene covalent and van der Waals junctions, J. Appl. Phys. **118**, 044302 (2015).

[31] N. Q. Le, C. A. Polanco, R. Rastgarkafshgarkolaei, J. Zhang, A. W. Ghosh, and P. M. Norris, Effects of bulk and interfacial anharmonicity on thermal conductance at solid/solid interfaces, Phys. Rev. B **95**, 245417 (2017).

[32] E. Lee and T. Luo, Thermal transport across solid-solid interfaces enhanced by pre-interface isotope-phonon scattering, Appl. Phys. Lett. **112**, 011603 (2018).

[33] J. Maassen and V. Askarpour, Phonon transport across a Si-Ge interface: The role of inelastic bulk scattering, APL Mater. **7**, 013203 (2019).

[34] Y. Guo, Z. Zhang, M. Bescond, S. Xiong, M. Nomura, and S. Volz, Anharmonic phonon-phonon scattering at the interface between two solids by nonequilibrium Green's function formalism, Phys. Rev. B **103**, 174306 (2021).

[35] P. E. Hopkins, J. A. Tomko, and A. Giri, Quasi-harmonic theory for phonon thermal boundary conductance at high temperatures, J. Appl. Phys. **131**, 015101 (2022).

[36] J. Han, H. T. Aller, and A. J. H. McGaughey, Quantifying atomic structural disorder using procrustes shape analysis, arXiv:2303.04108.

[37] See Supplemental Material at http://link.aps.org/supplemental/10.1103/PhysRevB.109.165421 for full details on sample and transducer preparation, ion damage prediction, thermoreflectance experiments and uncertainty analysis, alternative analysis schemes used to account for a depth-varying damage profile, NEMD simulation parameters, SHF calculations for the nonpairwise potential used, the Procrustes shape analysis procedure, tabulated ion energy and dosage information, assumptions for thermal measurement analysis, and TBR and thermal conductivity values. The Supplemental Material also contains Refs. [64–81].

[38] D. G. Cahill, Analysis of heat flow in layered structures for time-domain thermoreflectance, Rev. Sci. Instrum. **75**, 5119 (2004).

[39] A. J. Schmidt, R. Cheaito, and M. Chiesa, A frequency-domain thermoreflectance method for the characterization of thermal properties, Rev. Sci. Instrum. **80**, 094901 (2009).

[40] P. Jiang, X. Qian, and R. Yang, Tutorial: Time-domain thermoreflectance (TDTR) for thermal property characterization of bulk and thin film materials, J. Appl. Phys. **124**, 161103 (2018).

[41] J. F. Ziegler, M. D. Ziegler, and J. P. Biersack, Nuclear instruments and methods in Physics Research B SRIM –The stopping and range of ions in matter (2010), Nucl. Instrum. Methods Phys. Res. B **268**, 1818 (2010).

[42] A. Giri, J. P. Niemelä, C. J. Szwejkowski, M. Karppinen, and P. E. Hopkins, Reduction in thermal conductivity and tunable heat capacity of inorganic/organic hybrid superlattices, Phys. Rev. B **93**, 024201 (2016).

[43] K. Chen, B. Song, N. K. Ravichandran, Q. Zheng, X. Chen, H. Lee, H. Sun, S. Li, G. A. G. U. Gamage, F. Tian, Z. Ding, Q. Song, A. Rai, H. Wu, P. Koirala, A. J. Schmidt, K. Watanabe, B. Lv, Z. Ren, L. Shi *et al.*, Ultrahigh thermal conductivity in isotope-enriched cubic boron nitride, Science **367**, 555 (2020).

[44] J. P. Feser and D. G. Cahill, Probing anisotropic heat transport using time-domain thermoreflectance with offset laser spots, Rev. Sci. Instrum. **83**, 104901 (2012).

[45] H. Babaei, M. E. DeCoster, M. Jeong, Z. M. Hassan, T. Islamoglu, H. Baumgart, A. J. H. McGaughey, E. Redel, O. K. Farha, P. E. Hopkins, J. A. Malen, and C. E. Wilmer, Observation of reduced thermal conductivity in a metal-organic framework due to the presence of adsorbates, Nat. Commun. **11**, 4010 (2020).

[46] R. J. Stevens, L. V. Zhigilei, and P. M. Norris, Effects of temperature and disorder on thermal boundary conductance at solid-solid interfaces: Nonequilibrium molecular dynamics simulations, Int. J. Heat Mass Transf. **50**, 3977 (2007).

[47] Z. Tian, K. Esfarjani, and G. Chen, Enhancing phonon transmission across a Si/Ge interface by atomic roughness: First-principles study with the Green's function method, Phys. Rev. B **86**, 235304 (2012).

[48] Z. Liang and P. Keblinski, Finite-size effects on molecular dynamics interfacial thermal-resistance predictions, Phys. Rev. B **90**, 075411 (2014).

[49] F. Mu, Z. Cheng, J. Shi, S. Shin, B. Xu, J. Shiomi, S. Graham, and T. Suga, High thermal boundary conductance across bonded heterogeneous GaN-SiC interfaces, ACS Appl. Mater. Interfaces **11**, 33428 (2019).

[50] A. P. Thompson, H. M. Aktulga, R. Berger, D. S. Bolintineanu, W. M. Brown, P. S. Crozier, P. J. in 't Veld, A. Kohlmeyer, S. G. Moore, T. D. Nguyen, R. Shan, M. J. Stevens, J. Tranchida, C. Trott, and S. J. Plimpton, LAMMPS: A flexible simulation tool for particle-based materials modeling at the atomic, meso, and continuum scales, Comput. Phys. Commun. **271**, 108171 (2022).

[51] L. Pelaz, L. A. Marqús, and J. Barbolla, Ion-beam-induced amorphization and recrystallization in silicon, J. Appl. Phys. **96**, 5947 (2004).

[52] K. R. C. Mok, M. Jaraiz, I. Martin-Bragado, J. E. Rubio, P. Castrillo, R. Pinacho, J. Barbolla, and M. P. Srinivasan, Ion-beam amorphization of semiconductors: A physical model based on the amorphous pocket population, J. Appl. Phys. **98**, 046104 (2005).

[53] D. P. Hickey, K. S. Jones, and R. G. Elliman, Amorphization and graphitization of single-crystal diamond - A transmission electron microscopy study, Diam. Relat. Mater. **18**, 1353 (2009).

[54] S. K. Ghandhi, *VLSI Fabrication Principles: Silicon and Gallium Arsenide*, 2nd ed. (Wiley, 1995), Vol. 46, pp. 368–369.

[55] Y. Chalopin, K. Esfarjani, A. Henry, S. Volz, and G. Chen, Thermal interface conductance in Si/Ge superlattices by equilibrium molecular dynamics, Phys. Rev. B **85**, 195302 (2012).

[56] A. Giri, J. L. Braun, and P. E. Hopkins, Implications of interfacial bond strength on the spectral contributions to thermal boundary conductance across solid, liquid, and gas interfaces: A molecular dynamics study, J. Phys. Chem. C **120**, 24847 (2016).

[57] K. Sääskilahti, J. Oksanen, J. Tulkki, and S. Volz, Spectral mapping of heat transfer mechanisms at liquid-solid interfaces, Phys. Rev. E **93**, 052141 (2016).

[58] Z. Fan, H. Dong, A. Harju, and T. Ala-nissila, Homogeneous nonequilibrium molecular dynamics method for heat transport and spectral decomposition with many-body potentials, Phys. Rev. B **99**, 064308 (2019).

[59] R. Li, K. Gordiz, A. Henry, P. E. Hopkins, E. Lee, and T. Luo, Effect of light atoms on thermal transport across solid-solid interfaces, Phys. Chem. Chem. Phys. **21**, 17029 (2019).

[60] A. J. Gabourie, Z. Fan, T. Ala-Nissila, and E. Pop, Spectral decomposition of thermal conductivity: Comparing velocity decomposition methods in homogeneous molecular dynamics simulations, Phys. Rev. B **103**, 205421 (2021).

[61] T. Zhou, H. K. Chilukoti, Z. Wu, and F. Müller-Plathe, Effect of defects on the interfacial thermal conductance between n-Heneicosane in solid and liquid phases and a graphene monolayer, J. Phys. Chem. C **125**, 14149 (2021).

[62] K. Gordiz and A. Henry, Phonon transport at crystalline Si/Ge interfaces: The role of interfacial modes of vibration, Sci. Rep. **6**, 23139 (2016).

[63] E. A. Scott, K. Hattar, C. M. Rost, J. T. Gaskins, M. Fazli, C. Ganski, C. Li, T. Bai, Y. Wang, K. Esfarjani, M. Goorsky, and P. E. Hopkins, Phonon scattering effects from point and extended defects on thermal conductivity studied via ion irradiation of crystals with self-impurities, Phys. Rev. Mater. **2**, 095001 (2018).

[64] J. L. Braun and P. E. Hopkins, Upper limit to the thermal penetration depth during modulated heating of multilayer thin films with pulsed and continuous wave lasers: A numerical study, J. Appl. Phys. **121**, 175107 (2017).

[65] J. L. Braun, C. J. Szwejkowski, A. Giri, and P. E. Hopkins, On the steady-state temperature rise during laser heating of multilayer thin films in optical pump probe techniques, J. Heat Transfer **140**, 052801 (2018).

[66] J. L. Braun, D. H. Olson, J. T. Gaskins, and P. E. Hopkins, A steady-state thermoreflectance method to measure thermal conductivity, Rev. Sci. Instrum. **90**, 024905 (2019).

[67] Z. Fan, L. F. C. Pereira, H. Q. Wang, J. C. Zheng, D. Donadio, and A. Harju, Force and heat current formulas for many-body potentials in molecular dynamics simulations with applications to thermal conductivity calculations, Phys. Rev. B **92**, 094301 (2015).

[68] C. Moulet and M. S. Goorsky, Lattice strain measurements in hydrogen implanted materials for layer transfer processes, *Ion Implantation* (InTech, 2012), pp. 65–88.

[69] T. W. Pfeifer, J. A. Tomko, E. Hoglund, E. A. Scott, K. Hattar, K. Huynh, M. Liao, M. Goorsky, and P. E. Hopkins, Measuring sub-surface spatially varying thermal conductivity of silicon implanted with krypton, J. Appl. Phys. **132**, 075112 (2022).

[70] E. A. Scott, K. Hattar, J. L. Braun, C. M. Rost, J. T. Gaskins, T. Bai, Y. Wang, C. Ganski, M. Goorsky, and P. E. Hopkins, Orders of magnitude reduction in the thermal conductivity of polycrystalline diamond through carbon, nitrogen, and oxygen ion implantation, Carbon **157**, 97 (2020).

[71] E. A. Scott, J. L. Braun, K. Hattar, J. D. Sugar, J. T. Gaskins, M. Goorsky, S. W. King, and P. E. Hopkins, Probing thermal conductivity of subsurface, amorphous layers in irradiated diamond, J. Appl. Phys. **129**, 055307 (2021).

[72] E. A. Scott and P. E. Hopkins, Thermal conductivity manipulation through structural modification with ion beams, Ph.D. thesis, University of Virginia, Mechanical and Aerospace Engineering—School of Engineering and Applied Science, 2021.

[73] E. A. Scott, K. Hattar, E. J. Lang, K. Aryana, J. T. Gaskins, and P. E. Hopkins, Reductions in the thermal conductivity of irradiated silicon governed by displacement damage, Phys. Rev. B **104**, 134306 (2021).

[74] Y. S. Touloukian and E. H. Buyco, *Specific Heat — Metallic Elements and Alloys*, Thermophysical Properties of Matter: TPRC Data Series, Vol. 4 (1970), p. 832.

[75] Y. S. Touloukian and E. H. Buyco, *Specific Heat — Nonmetallic Solids*, Thermophysical properties of matter: The TPRC data series, Vol. 5 (1970), p. 25.

[76] Y. S. Touloukian, R. W. Powell, C. Y. Ho, and P. G. Klemens, *Thermophysical Properties of Matter: Thermal Conductivity of Nonmetallic Solids* (1970), pp. 30–37.

[77] Y. Wang, J. Y. Park, Y. K. Koh, and D. G. Cahill, Thermoreflectance of metal transducers for time-domain thermoreflectance, J. Appl. Phys. **108**, 043507 (2010).

[78] Y. Wang, K. Huynh, M. E. Liao, H. M. Yu, T. Bai, J. Tweedie, M. H. Breckenridge, R. Collazo, Z. Sitar, M. Bockowski, Y. Liu, and M. S. Goorsky, Strain recovery and defect characterization in Mg-implanted homoepitaxial GaN on high-quality GaN substrates, Physica Status Solidi (b) **257**, 1900705 (2020).

[79] K. Wittmaack, Misconceptions impairing the validity of the stopping power tables in the SRIM library and suggestions for doing better in the future, Nucl. Instrum. Methods Phys. Res. Sect. B **380**, 57 (2016).

[80] Z. Xiang, Y. Pang, X. Qian, and R. Yang, Machine learning reconstruction of depth-dependent thermal conductivity profile from pump-probe thermoreflectance signals, Appl. Phys. Lett. **122**, 142201 (2023).

[81] Y. Zhang, I. T. Bae, K. Sun, C. Wang, M. Ishimaru, Z. Zhu, W. Jiang, and W. J. Weber, Damage profile and ion distribution of slow heavy ions in compounds, J. Appl. Phys. **105**, 104901 (2009).